ADVANCED SUSTAINABLE SYSTEMS
www.advsustainsys.com

High Shunt Resistance SnO_2-PbO Electron Transport Layer for Perovskite Solar Cells Used in Low Lighting Applications

Zhuoneng Bi, Shaohong Zhang, Marimuthu Thandapani, Yanqing Zhu, Yupeng Zheng, Nguyen Quang Liem, Xiudi Xiao, Gang Xu, Antonio Guerrero, and Xueqing Xu**

Hybrid perovskites are promising materials for new sustainable photovoltaic applications to operate under low lighting conditions, such as the reuse of residual photons that are wasted during indoor lighting. The requirements for a perovskite solar cell (PSC) to offer maximum power conversion efficiency (PCE) under low illumination conditions are not totally clear in the literature. In this work, the PCE of the commonly used SnO_2 electron transport layer (ETL) is improved by a facile method, doping the precursor nanoparticles with small concentrations of a Pb source. Under low illumination conditions (i.e., 0.1 mW cm^{-2}) the PCE is enhanced from 18.8% to 34.2%. From a complete analysis of the ETLs and devices using several structural and electrical techniques it is observed that the parameter that improves the most is the shunt resistance of the device which avoids the parallel leakage of the photogenerated current. The present work clearly shows that the shunt resistance is a very important parameter that needs to be optimized in PSCs for low illumination conditions.

1. Introduction

Perovskite solar cells (PSCs) have received much attention due to the impressive power conversion efficiencies (PCE) with record value of 25.5% under standard 1 sun illumination conditions (AM1.5G, 100 mW cm^{-2}).[1] With these efficiencies PSCs not only find applications as solar panels installed in large solar farms that may compete with silicon technology but also show promising compatibility with light-weight and flexible devices produced at reduced costs.

A large array of new applications may be developed using PSCs which could contribute toward a sustainable energy model.[2–5] Due to the compatibility with light weight substrates innovative consumer applications are envisaged including wearable photovoltaics and decorative construction elements that reuse the residual photons wasted during indoor lighting. Several photovoltaic technologies have been developed to operate under low illumination intensities, i.e., 1000 lux corresponds to ≈1 mW cm^{-2} for LED lighting. For example, dye-sensitized solar cells and organic photovoltaics have demonstrated PCEs approaching ≈32%[6] and ≈28%,[7] respectively. Still higher PCEs have been obtained at low illumination conditions using PCSs. For example, Wang and Liao et al. achieved excellent PSCs of ≈20% and ≈35% under one sun illumination and under indoor condition (1000 lux), respectively.[8] The general approach has been to improve either the perovskite formulation or the extraction layers. However, the specific rules to design PSCs for low lighting conditions have not been discussed in terms of the different layers that compose a photovoltaic device.

The properties of electron transport layers (ETL) designed for operation under high illumination conditions are well stablished and these include adequate energy levels and high electron mobility. Tin oxide (SnO_2) is one of the most widely used ETL due to the versatile processing conditions as it may be deposited as a compact layer, mesoporous layer or as a modifier by several techniques.[9–15] PCEs exceeding 20% have been obtained under 1 sun illumination conditions using perovskite formulations.[14] Unfortunately, under low illumination conditions (i.e., 1000 lux) devices prepared with SnO_2 generally provide relatively low PCE of 20.2% with V_{oc} and *FF* being the most affected parameters.[16]

Z. Bi, S. Zhang, Dr. M. Thandapani, Dr. Y. Zhu, Y. Zheng, Prof. X. Xiao, Prof. G. Xu, Prof. X. Xu
Key Laboratory of Renewable Energy
Guangdong Key Laboratory of New and Renewable Energy Research and Development
Guangzhou Institute of Energy Conversion
Chinese Academy of Sciences
Guangzhou 510640, China
E-mail: xuxq@ms.giec.ac.cn

Z. Bi, S. Zhang, Y. Zheng, Prof. X. Xiao, Prof. G. Xu, Prof. X. Xu
Center of Materials Science and Optoelectronics Engineering
University of Chinese Academy of Sciences
Beijing 100049, China

Prof. N. Q. Liem
Institute of Materials Science
VAST, Hanoi 100803, Vietnam

Prof. A. Guerrero
Institute of Advanced Materials (INAM)
Universitat Jaume I, Castelló 12006, Spain
E-mail: aguerrer@uji.es

The ORCID identification number(s) for the author(s) of this article can be found under https://doi.org/10.1002/adsu.202100120.

DOI: 10.1002/adsu.202100120

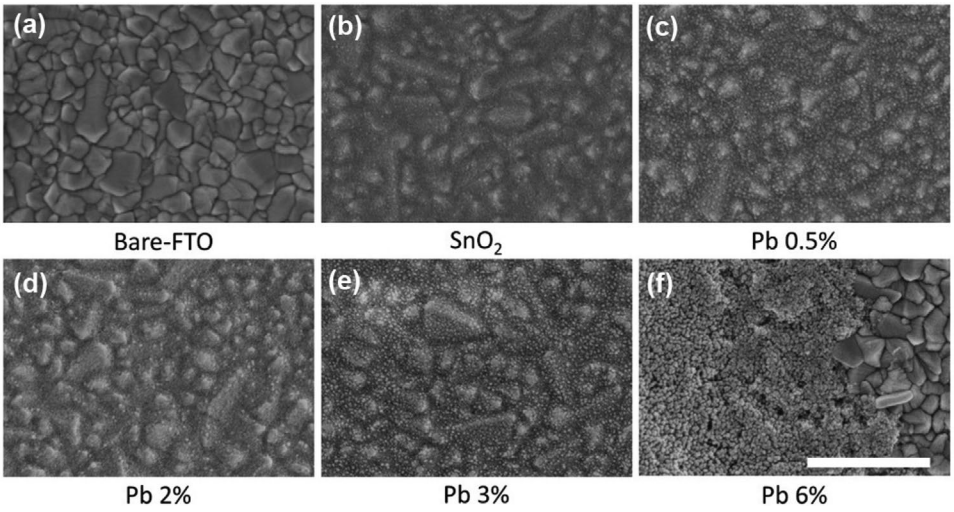

Figure 1. Top-view SEM images of the SnO_2 with different Pb doping, the scale bar is 500 nm.

The use of SnO/ZnO bilayers as ETLs are effective to improve PCE to values of 37.2% and improves the stability using the same conditions. The PCE improvement of the bilayers was ascribed to a suppression of the trap-assisted recombination. However, the role of the leakage current and shunt resistance have not been clarified which should be one of the most important parameters for low illumination conditions as discussed by Proctor et al. in the field of organic photovoltaics.[17] In particular, the V_{oc} and FF should be strongly affected by a variation in the shunt resistance.

In this work, we introduce a PbO precursor into SnO_2 nanoparticles that forms an ETL layer that greatly enhance the PCEs of photovoltaic devices measured under low illumination conditions. The ETL narrows the bandgap of pure SnO_2 and increases the shunt resistance of devices that avoids the leakage of photogenerated current. It is found that ETLs containing SnO_2/PbO shows excellent performance with perovskite formulation prepared by blade-coating (compatible with roll-to-roll production methods),[18] best PCE of 18.8% (1 sun) and 34.2% (0.1 mW cm^{-2}) under white-light LED illumination. Very importantly, we highlight the effect of the shunt resistance on the V_{OC} and *FF* of the devices used under low illumination intensity.

2. Results and Discussion

2.1. Characterization of Layers Containing SnO_2-PbO on Fluorine-doped Tin Oxide (FTO)

Layers of SnO_2 nanoparticles containing PbO were prepared by a simple method, such as spin coating of mixtures of SnO_2 nanoparticles with lead acetate. A detailed synthesis is explained in the experimental section and incorporation of PbO into the nanoparticles are confirmed by a range of techniques as described next. The molar ratio of Pb to Sn was varied from 0.5% to 6%. The top-view scanning electron microscope (SEM) images (**Figure 1**) shows reference samples containing bare FTO and FTO/SnO_2. As can be observed, SnO_2 covers homogeneously the FTO and aggregates slightly. Alternatively, in the presence of Pb the morphology of the thin film is modified with relevant aggregation of particles increasing with the proportion of lead acetate in the precursor solution. With the highest Pb concentration of 6% the FTO film cannot be fully covered due to the severe aggregation of the nanoparticles.

X-ray diffraction (XRD) was measured (**Figure 2**a) on films deposited on glass using the conditions described above. As expected, the SnO_2 shows a tetragonal structure (JCPDS No. 01-072-1147) with most relevant peaks appearing at 2θ = 26.6, 33.8, and 52.1 that can be associated with (110), (101), (211) planes, respectively. The Pb precursor does not greatly modify the SnO_2 tetragonal structure.[19] However, the structure gets distorted as the Pb concentration increases as noted by the decrease in the intensity of (110) planes and by the shift of the peaks to lower 2θ values. The second observation indicates that introduction of Pb into the lattice increases the interplanar crystal spacing as expected by the replacement of some Sn atoms by the larger Pb atom. Further supporting the incorporation of Pb into the SnO_2 lattice we show transmission electron microscopy analysis as Supporting Information.

X-ray photoelectron spectroscopy (XPS) shows the surface composition of the layers and helps to determine the oxidation state of Sn, Pb, and O. Figure 2b displays the $Sn3d_{5/2}$ and $Sn3d_{3/2}$ spectra of SnO_2 and samples containing Pb. The binding energies (BE) of the $Sn3d_{5/2}$ and $Sn3d_{3/2}$ are very similar in all samples except sample containing Pb-6% which was shown in the SEM images to show an anomaly behavior. Figure 2c shows the $Pb4f_{5/2}$ and $Pb4f_{7/2}$ and Sn4s spectra of all samples. The Sn4s peaks overlap with $Pb4f_{7/2}$ at BE of 138.4 for the Pb doped samples. When the Pb-doping concentration increases from 0.5% to 6%, the $Pb4f_{7/2}$ fitting peak shifts from BE 138.3 to 138.6, respectively. As the BE of the $Pb4f_{7/2}$ of Pb native oxide (PbO) is 138.4 we confirm that PbO is present in all samples as observed in Figure 2d.[20] As expected, the intensity of the signal increases with the increased Pb concentration. The quantitative analysis of Pb:Sn ratio and each Atomic-% is shown in the Table S1 (Supporting Information). As can be observed in Figure 2e, there is a small variation in the valence band edge position decreasing from 3.32 to 2.95 eV when comparing SnO_2 with increasing amounts of Pb concentration.[21] The current results suggests that Pb introduction into the nanoparticles leads to a reduction in valence band edge, further XPS analysis

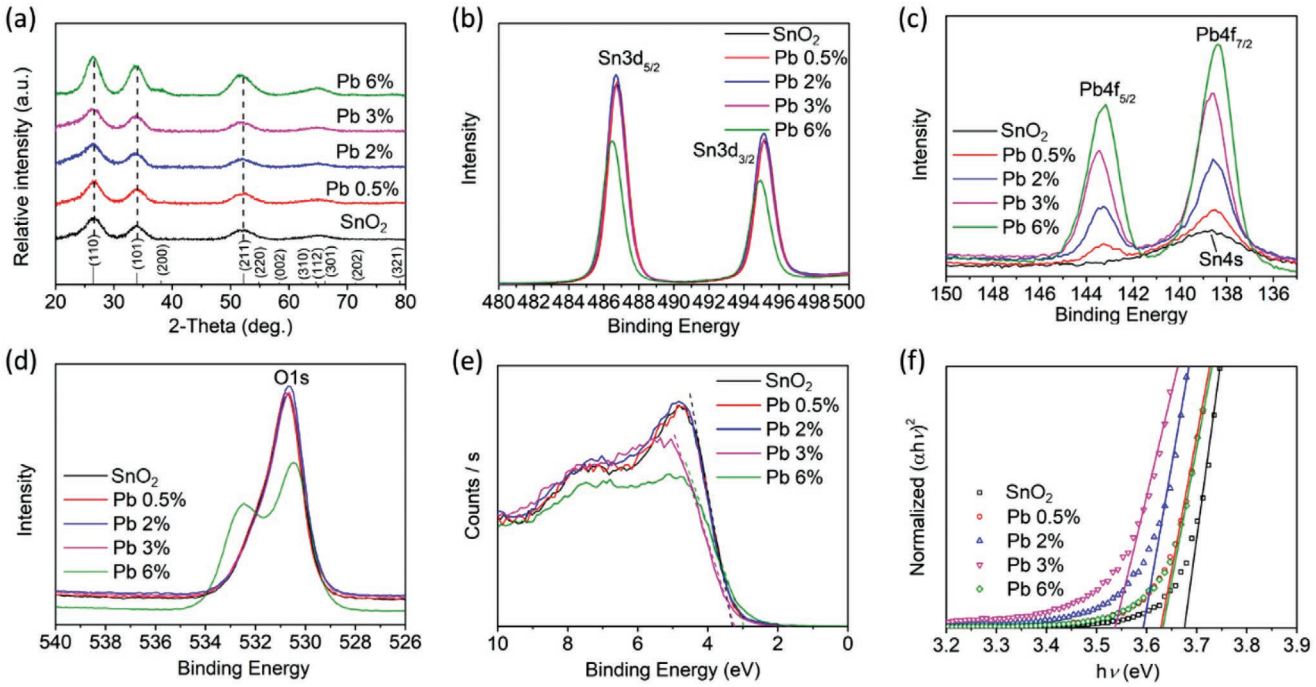

Figure 2. a) XRD patterns. b) XPS spectra depicting the Sn 3d3/2, Sn 3d5/2 peaks. c) XPS spectra depicting the Pb4f5/2, Pb4f7/2 peaks, d) XPS spectra depicting the O 1s peaks. e) The valence spectrum. f) Normalized $(\alpha h\nu)^2$ versus $h\nu$ plot of pure and Pb doped SnO_2 layer on glass. All the binding energies are referenced to the C1s peak at 284.8 eV.

is shown as the Supporting Information. The work function and valence band maximum (VBM) measurements were carried out by ultraviolet photoelectron spectroscopy (UPS) and the results are shown in Figure S5 (Supporting Information).[22] Finally, the optical energy bandgap (Eg) was evaluated from the UV–vis absorption spectra by using the direct interband absorption gap, as shown in Figure 2f. The bandgap of samples can be calculated by extrapolating the linear portion of the $(\alpha h\nu)^2$ versus $h\nu$ curve to zero where $h\nu$ is the photon energy.[19] Importantly, it is found that the bandgap is slightly reduced from 3.67 to 3.53 eV with the increase in Pb concentration up to 3%. The energy levels of the prepared ETL are shown in **Figure 3**a which shows adequate values to extract electrons from the perovskite layer.

2.2. Device Fabrication and Characterization of Photovoltaic Devices Using $MAPbI_3$ Formulation Deposited on SnO_2-PbO

High quality $MAPbI_3$ perovskite was deposited by doctor blade onto the SnO_2 ETL layer containing 3% of PbO,[23] a deposition method compatible with industrially relevant methods such as roll-to-roll. Complete optimization conditions of the deposition process and characterization of the layers are shown as the Supporting Information. As previously reported the $MAPbI_3$ film shows spherulitic morphology and fully covers the surface of the ETL. Photovoltaic devices have been prepared in the configuration shown in Figure 3, Glass/FTO/SnO_2-PbO/$MAPbI_3$/Spiro-OMeTAD/Au. Cross-section SEM images clearly show

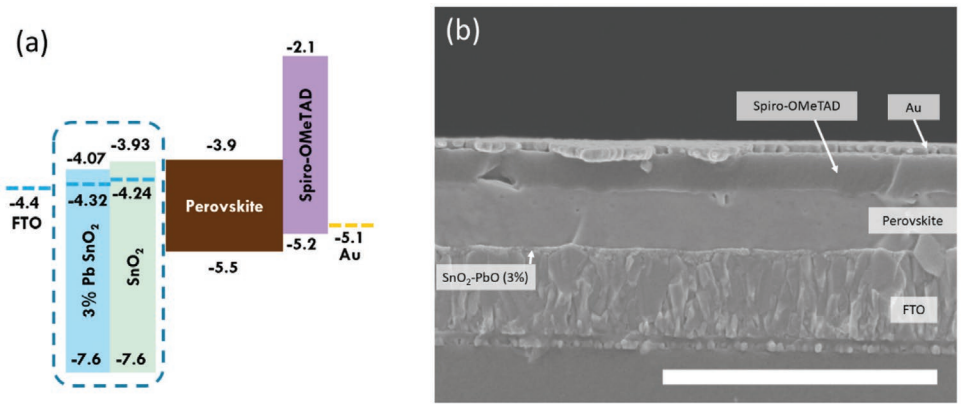

Figure 3. a) Schematic energy level diagram of the complete device including the SnO_2-PbO ETL. b) Cross-section SEM image of the SnO_2-PbO ETLs based PSCs, the scale bar is 1 μm.

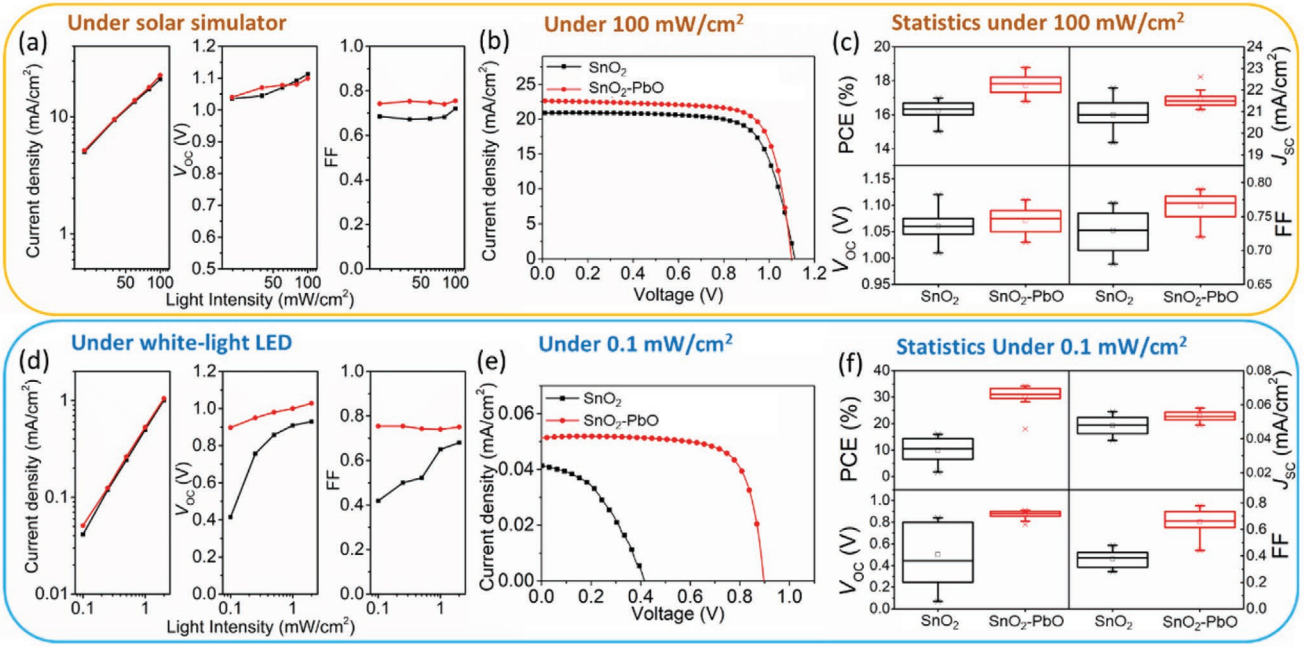

Figure 4. a) J_{SC}, V_{OC}, and FF versus light intensity using a solar simulator (AM 1.5 G). b) *J–V* curves measured at 100 mW cm^{-2}. c) Statistics of 20 controls (SnO_2) and 20 bilayer SnO_2-PbO ETLs-based devices under AM 1.5. d) J_{SC}, V_{OC}, and *FF* versus light intensity under white-light LED. e) *J–V* curves under 0.1 mW cm^{-2} white-light LED. f) Statistics of 20 controls (SnO_2) and 20 bilayer SnO_2-PbO ETLs-based devices under 0.1 mW cm^{-2} white-light LED.

that $MAPbI_3$ films benefit from very large grains without the presence of any pin holes. In addition, the ETL thickness is measured to be in the range between 30 and 50 nm.

The photovoltaic properties have been analyzed under different light sources. The results of measurements under high light intensity conditions using a solar simulator (AM 1.5 G) are shown in **Figure 4**a–c as a function of the light intensity, from 100 to 10 mW cm^{-2}. At these relatively high illumination conditions the response of the devices show expected results with a direct relationship between light intensity (photogeneration) and extracted current density, a small decrease in V_{oc} and similar FF at the different lighting conditions. Figure 4b shows *J–V* curves at 1 sun light intensity (100 mW cm^{-2}) for both samples where it can be observed that there is a modest improvement in the *J–V* response for SnO_2-PbO as compared to the reference SnO_2 sample. Statistics over 20 devices (Figure 4c) measured at 100 mW cm^{-2} show a modest improvement in PCE from 16.2% to 17.7% when PbO is incorporated into the SnO_2 layer. Reduced *FF* and photocurrents are observed for the sample which does not contain PbO. Analogous measurements were carried out using a white-light LED at still lower light intensities from 0.1 to 10 mW cm^{-2} (Figure 4d–f). Figure 4d shows a large variation in the performance parameters as a function of the light intensity between the two samples. Whilst the SnO_2-PbO follows a similar behavior to results measured under high illumination conditions the reference SnO_2 sample shows inferior V_{oc} and *FF*. The *J–V* curves of representative solar cells at 0.1 mW cm^{-2} (≈285 Lux) under a white-light LED are displayed in Figure 4e. Results, clearly highlight the poor performance of the SnO_2 sample with a V_{oc} of only 0.4 V, with results similar to those reported by other authors.[16] Statistics over 20 devices measured at 0.1 mW cm^{-2} (Figure 4f) highlights a marked difference between SnO_2 and SnO_2-PbO with average PCE of 10.1% and 30.3%, respectively. The origin of this remarkable improvement in performance will be analyzed below.

2.3. Origin of Improved Performance of Devices Containing SnO_2-PbO

We believe that the improved performance observed under low illumination conditions for ETLs containing SnO_2-PbO is related to formation of PbO at the interface with the perovskite that increases the shunt resistance of the device. PbO is known to be highly resistive with bulk resistance values of about 10^7 Ω.[24] In our work, generation of a thin layer of PbO should be sufficient to increase the shunt resistance and block the extraction of undesired leakage current. In order to test this hypothesis, we have completed a set of electrical measurements.

First, devices in the configuration FTO/ETL/Au have been prepared and *J–V* curves (**Figure 5**a) and impedance spectroscopy (Figure 5b) have been measured in the dark at voltages close to 0 V. The introduction of PbO increases the series resistance of the device reducing the current that can be driven through the SnO_2/PbO layer. The shunt resistance (R_{sh}) cannot be measured by impedance spectroscopy itself as R_{sh} belongs to a parallel subcircuit. However, the measurement provides two pieces of valuable information: 1) The series resistance increases, as directly observed from the intercept with the *x*-axis, when PbO is present in the layer with values of ≈6 Ω as compared to with values of ≈5 Ω for SnO_2. 2) The observed arc provides information on the charge transfer resistance from the electrode to the ETL with values of ≈5 Ω for the SnO_2/PbO and ≈2 Ω for the SnO_2. This increased charge transfer resistance

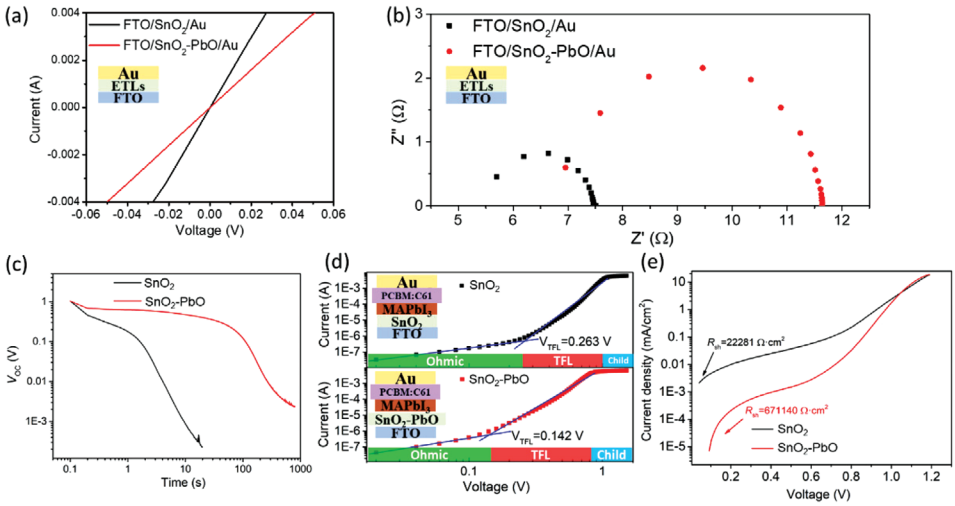

Figure 5. a) *J–V* curves and b) Impedance spectroscopy measured in the dark of devices in the configuration of FTO/ETL/Au. c) Open-circuit voltage decay of SnO_2 and SnO_2-PbO ETLs based PSCs. d) Dark *J–V* cures of electron-only device with a configuration of FTO/SnO_2 or SnO_2-PbO ETLs / perovskite/PCBM/Au. e) *J–V* curves measured in the dark and extraction of R_{sh}.

observed for SnO_2/PbO will be the origin of the increased shunt resistance in photovoltaic devices which avoids the leakage of current.

In addition, open-circuit voltage decay (OCVD) measurements were carried out by illumination at 1 sun light intensity, the illumination is turned off within 100 ms by using a shutter and results are shown in Figure 5c. In agreement with previously reported results for the reference SnO_2 the device polarization leads to accumulation of charge and depolarization process is around ≈10–100 s.[25,26] Alternatively, the SnO_2-PbO shows that depolarization occurs significantly slower in the range of 500–1000 s. This result points to depolarization of the device via a slow leakage of the charge due to a reduced parallel current pathway related shunt resistance (R_{sh}) as discussed below. While devices containing SnO_2 suffer from a low R_{sh} (increased parallel pathways) the SnO_2-PbO benefit from high R_{sh}. To rule out effects of charge transport inside the ETL the electron mobility was measured using the space charge-limited current (SCLC) method,[27] as shown in Figure 5d. In trap-free Child' s region, forming space charge limited current, the dark current was well fitted by the Mott–Gurney law

$$J_D = \frac{9\varepsilon\varepsilon_0\mu V_b^2}{8L^3} \quad (1)$$

Where J_D is the dark current density of devices, V_b is applied voltage, L (≈500 nm) is the thickness between two electrodes, ε_0 is the vacuum permittivity, ε (= 32) is relative dielectric constant of $MAPbI_3$, μ is the carrier mobility. Using this technique, it is found that electron mobility is only slightly improved from of 6.52×10^{-4} cm^2 V^{-1} s^{-1} for SnO_2 as compared to 1.07×10^{-3} cm^2 V^{-1} s^{-1} for SnO_2-PbO samples. Similar conclusions are obtained using steady state photoluminescence (PL) and time-resolved photoluminiscence (TRPL) as discussed in supporting information with charge lifetimes of 12.44 and 8.74 ns for SnO_2 and SnO_2-PbO, respectively. The shorter PL lifetime and significant PL quenching for the SnO_2-PbO confirms its slightly superior electron extraction ability but does not account for the significant difference in V_{oc} observed under low illumination conditions. Alternatively, the shunt resistance can be extracted from the *J–V* measured in dark (Figure 5e) using the single diode model as explained in the Supporting Information.[28] This parameters offer straight forward information on parallel charge pathways which do not contribute to the photocurrent. Results clearly show differences in R_{sh} of more than one order of magnitude with values of 22.3 and 671.1 kΩ cm^2 for SnO_2 and SnO_2-PbO, respectively.

We recall here that results using perovskite solar cells used for low illumination conditions ascribed efficiency improvement to reduced trap-assisted recombination but the current results point to a great enhancement in the R_{sh} similar to results observed in organic photovoltaic by Proctor.[17] For this reason, we next simulated *J–V* using the single diode model (**Figure 6**a) with the basic parameters defined as the reverse saturated current density (J_0), junction ideality factor (A), shunt resistance (R_{sh}), and series resistance (R_s).[29,30] Parameters are extracted from the devices and electrical measurements obtained in this work. As it can be observed, the *FF* and V_{oc} of the device is greatly affected by the shunt resistance under low-light conditions. This is because the photovoltage is a function of the light intensity (and photogenerated current) and in the extreme case at open circuit conditions the difference in potential between the two terminals cannot be maintained if there is a shunt current that shorts the device. At high light intensity there is still sufficient photogenerated current to maintain the photovoltage of the device but at low illumination conditions the shunt current and photogenerated current are comparable. The shunt loss rate can be defined as J_{sh}/J_{ph} and the shunting loss is more obvious under low-light condition. Hence, high R_{sh} is necessary for solar cells to work under low-light condition. If we use parameters extracted from the devices actually prepared in this work the model can be used to simulate different conditions in which R_{sh} changes significantly. Here, we used fixed parameters of $J_0 = 1 \times 10^{-11}$ mA cm^{-2}, A = 1.5, T = 310 K and

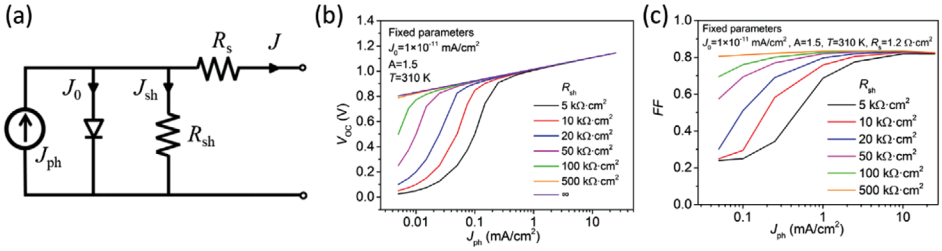

Figure 6. a) Equivalent circuit of solar cell. b,c) Simulated V_{OC}–J_{ph} and FF–J_{ph} curves as a function of the R_{sh} for different shunt resistances using the parameters shown in the panels.

$R_s = 1.2\ \Omega\ cm^2$. Figure 6b,c shows the results of the simulations where photogenerated current is plot with either V_{oc} or FF. If we consider the actual values of R_{sh} calculated from devices in this work, R_{sh} = 22 kΩ cm^2 for SnO_2 and 671 kΩ cm^2 for SnO_2-PbO, each device would correspond to blue and orange traces in the plots. Under these conditions it is clear that both the V_{oc} and FF are very sensitive to the R_{sh} and SnO_2-PbO ETL is well suited for photovoltaic devices used for low illumination conditions.

3. Conclusions

In summary, we presented a simple method to incorporate PbO into SnO_2 nanoparticles under low processing temperatures to form an ETL well suited for low illumination conditions photovoltaic devices. Doping the nanoparticles with Pb slightly improves the performance under 1 sun light illumination as compared to a reference device that only contains SnO_2. The performance of optimized devices approaches the maximum PCE obtained using the simple perovskite formulation based on $MAPbI_3$ (≈19%). Alternatively, the performance improvement under low illumination conditions (i.e., 0.1 mW cm^{-2}) is remarkable with PCE improving from 10.1% to 30.3% when the ETL layer is doped with a PbO precursor. Characterization of the ETLs and corresponding devices points that such a remarkable improvement is related to a large increase in the shunt resistance when PbO is incorporated. Simulation results clearly show the large impact of the R_{sh} for applications under low illumination conditions on the V_{OC} and FF. Therefore, Pb-doped SnO_2 nanoparticles are presented as a very promising ETL layer for low illumination conditions.

4. Experimental Section

Materials: PbI_2 (99.99%) and 4-tert-butylpyridine (TBP) were purchased from TCI. CH_3NH_3I (MAI) and Spiro-OMeTAD were purchased from Xi'an Polymer Light Technology Corp. The SnO_2 solution (tin (IV) oxide, 15 wt% in H_2O colloidal dispersion) was obtained from Alfa Aesar. $Pb(CH_3COO)_2{\cdot}3H_2O$ (99.99%) was obtained from Aladdin. dimethyl sulfoxide (DMSO), gamma-Butyrolactone (GBL) and lithium bis (trifluoromethanesulfonyl) imide (Li-TFSI) (99.95%) were purchased from Sigma-Aldrich Inc. Other materials were purchased from Aladdin.

Precursor Solutions: For ETL layers containing only SnO_2 the commercially available aqueous nanoparticle colloidal dispersion (15 wt%) was diluted to 2.5 wt% using deionized water. The solution was stirred at room temperature for 2 h. For ETLs containing PbO the $Pb(CH_3COO)_2{\cdot}3H_2O$ was dissolved in deionized water followed by addition of the SnO_2 aqueous colloidal dispersion (15 wt%), the Pb: Sn molar ratio was varied from 0.5% to 6%. These solutions were stirred in the atmosphere at room temperature for 12 h. The perovskite precursor solution was prepared by mixing GBL and DMSO solvents with PbI_2 and MAI (1.05: 1 mol%). The GBL: DMSO ratio was modified as required for optimization. In the best condition, the concentration of 1.2 M and 3: 2 volume ratio corresponding to PbI_2 580.9 mg, MAI 190.8 mg, GBL 600 µL, and DMSO 400 µL.

Device Fabrication: FTO-coated glass substrates (14 Ω/□) were patterned by etching with zinc powder and HCl (2 M). The etched substrates were ultrasonically cleaned with soap solution, deionized water, ethanol, and isopropanol, respectively, and then dried under a stream of nitrogen. The SnO_2 layer was spin coated onto the pre-cleaned FTO substrate using SnO_2 solution at 4000 rpm for 30 s, then, annealed on a hot plate at 90 °C for 10 min followed by 150 °C for 30 min. The SnO_2-PbO layer were deposited by two different methods, both display similar PCEs and behavior with light intensity. A single layer of SnO_2-PbO was prepared by deposition on FTO of the SnO_2 nanoparticles doped with lead acetate solution at 4000 rpm for 30 s followed by a thermal treatment at 150 °C during 1 h. A bilayer approach was also attempted. First, depositing and thermally treating Pb-doped SnO_2 solution as before, UV–O_3 treated for 15 min and followed by deposition of a second layer using the same conditions with the SnO_2 solution. Both methodologies show similar results. The ETLs-coated substrates were then treated in a UV–O_3 cleaner for 15 min before blade-coating perovskite film. The perovskite precursor solution (20 µL) was coated by using doctor blade coater at the substrate temperature of 155 °C. The gap between the blade and the substrate was 150 µm and the blade speed was 1 mm/s. The perovskite dark phase was formed within the first few seconds. Perovskite precursor deposition was performed in ambient conditions (R.H. 30% ~ 40%). The hole-transport material (HTM) solution was spin-coated onto the perovskite layer at 4000 rpm for 30 s, which was prepared by dissolving 72.3 mg of Spiro-OMeTAD, 28.8 µl of TBP, and 17.5 µl of Li-TFSI solution (520 mg Li-TFSI in 1 ml acetonitrile) in 1 ml of chlorobenzene. Finally, 50 nm thickness of gold layer was thermally evaporated on top of the Spiro-OMeTAD-coated film as a back contact.

Film and Device Characterization: Morphology and microstructural characterization were performed using an SU-70 High resolution analytical SEM (Hitachi, Japan). The X-ray diffraction (XRD) measurements were carried out on X'Pert PRO MPD X-ray diffractometer using Cu Kα irradiation at a scan rate (2θ) of 0.0167° S^{-1}. X-ray photoelectron spectroscopy (XPS) was performed on Thermo Scientific ESCALAB 250Xi instrument with Al Kα as the X-ray source. UPS was also carried out on a Thermo Scientific ESCALAB 250Xi, with the HeI (21.22 eV) emission line employed for excitation. The data were acquired at a bias of 0V to-25V. High-resolution transmission electron microscope (HRTEM) images were obtained using a JEOL-2100F TEM. Absorption spectra were recorded using a Perkin-Elmer Lambda 750 spectrophotometer. The PL spectrum and lifetime measurements of perovskite films were conducted on Edinburgh fluorescence spectrometers (FLS980). The current density-voltage (J-V) curves were measured using an Autolab TYPE II electrochemical work station. The

cells were illuminated using the ABET Sun 3000 solar simulator with a source meter (Keithley 2420) at 100 mA/cm^2 illumination (AM 1.5 G), where the light intensity was adjusted with an NREL calibrated silicon solar cell. The white light LED and indoor condition light intensity were measured using TENMARS TM-208. The devices and white light LED were placed in dark box at fixed distance. The light intensity was adjusted by changing the input current of LED using a calibrated photodiode. The solar cells were masked with an aperture to define the active area of 0.24 cm^2. All the measurements of the solar cells were performed under ambient atmosphere at room temperature without any encapsulation.

Supporting Information

Supporting Information is available from the Wiley Online Library or from the author.

Acknowledgements

This work was supported by the Project on Collaborative Innovation and Environmental Construction Platform of Guangdong Province (No. 2018A050506067). The authors also thank the financial support from the Key Laboratory of Renewable Energy, Chinese Academy of Sciences (No. y807j71001), Guangdong Provincial Key Laboratory of New and Renewable Energy Research and Development (Grant No. Y909kp1001), and the Key Project on Synergy Collaborative Innovation of Guangzhou City (No. 201704030069). University Jaume I is also acknowledged for financial support (No. UJI-B2020-49).

Conflict of Interest

The authors declare no conflict of interest.

Data Availability Statement

Research data are not shared.

Keywords

indoor applications, low illumination, perovskite solar cells, shunt resistance

Received: April 19, 2021
Revised: June 2, 2021
Published online:

[1] NREL, B. R.-C. E., https://www.nrel.gov/pv/cell-efficiency.html (accessed: 13 April 2021).
[2] H. J. Snaith, *J. Phys. Chem. Lett.* **2013**, *4*, 3623.
[3] M. A. Green, A. Ho-Baillie, H. J. Snaith, *Nat. Photonics* **2014**, *8*, 506.
[4] X. T. Hu, Z. Q. Huang, F. Y. Li, M. Su, Z. D. Huang, Z. P. Zhao, Z. R. Cai, X. Yang, X. C. Meng, P. W. Li, Y. Wang, M. Z. Li, Y. W. Chen, Y. L. Song, *Energy Environ. Sci.* **2019**, *12*, 979.
[5] X. T. Hu, F. Y. Li, Y. L. Song, *ACS Energy Lett.* **2019**, *4*, 1065.
[6] Y. M. Cao, Y. H. Liu, S. M. Zakeeruddin, A. Hagfeldt, M. Gratzel, *Joule* **2018**, *2*, 1108.
[7] H. K. H. Lee, J. Y. Wu, J. Barbe, S. M. Jain, S. Wood, E. M. Speller, Z. Li, F. A. Castro, J. R. Durrant, W. C. Tsoi, *J. Mater. Chem. A* **2018**, *6*, 5618.
[8] C. Dong, M. Li, Y. Zhang, K.-L. Wang, S. Yuan, F. Igbari, Y. Yang, X. Gao, Z.-K. Wang, L.-S. Liao, *ACS Appl. Mater. Interfaces* **2020**, *12*, 836.
[9] L. B. Xiong, Y. X. Guo, J. Wen, H. R. Liu, G. Yang, P. L. Qin, G. J. Fang, *Adv. Funct. Mater.* **2018**, *28*, 1802757.
[10] E. H. Anaraki, A. Kermanpur, L. Steier, K. Domanski, T. Matsui, W. Tress, M. Saliba, A. Abate, M. Gratzel, A. Hagfeldt, J. P. Correa-Baena, *Energy Environ. Sci.* **2016**, *9*, 3128.
[11] Q. Jiang, L. Q. Zhang, H. L. Wang, X. L. Yang, J. H. Meng, H. Liu, Z. G. Yin, J. L. Wu, X. W. Zhang, J. B. You, *Nat. Energy* **2017**, *2*, 16177.
[12] J. P. C. Baena, L. Steier, W. Tress, M. Saliba, S. Neutzner, T. Matsui, F. Giordano, T. J. Jacobsson, A. R. S. Kandada, S. M. Zakeeruddin, A. Petrozza, A. Abate, M. K. Nazeeruddin, M. Gratzel, A. Hagfeldt, *Energy Environ. Sci.* **2015**, *8*, 2928.
[13] K. Liu, S. Chen, J. H. Wu, H. Y. Zhang, M. C. Qin, X. H. Lu, Y. F. Tu, Q. B. Meng, X. W. Zhan, *Energy Environ. Sci.* **2018**, *11*, 3463.
[14] M. M. Tavakoli, F. Giordano, S. M. Zakeeruddin, M. Gratzel, *Nano Lett.* **2018**, *18*, 2428.
[15] X. Gong, Q. Sun, S. S. Liu, P. Z. Liao, Y. Shen, C. Gratzel, S. M. Zakeeruddin, M. Gratzel, M. K. Wang, *Nano Lett.* **2018**, *18*, 3969.
[16] Y. W. Noh, I. S. Jin, K. S. Kim, S. H. Park, J. W. Jung, *J. Mater. Chem. A* **2020**, *8*, 17163.
[17] C. M. Proctor, T. Q. Nguyen, *Appl. Phys. Lett.* **2015**, *106*, 083301.
[18] F. Huang, M. J. Li, P. Siffalovic, G. Z. Cao, J. J. Tian, *Energy Environ. Sci.* **2019**, *12*, 518.
[19] S. N. Sarangi, G. K. Pradhan, D. Samal, *J. Alloy Compd.* **2018**, *762*, 16.
[20] D. J. Payne, R. G. Egdell, W. Hao, J. S. Foord, A. Walsh, G. W. Watson, *Chem. Phys. Lett.* **2005**, *411*, 181.
[21] H. K. Wang, K. P. Dou, W. Y. Teoh, Y. W. Zhan, T. F. Hung, F. H. Zhang, J. Q. Xu, R. Q. Zhang, A. L. Rogach, *Adv. Funct. Mater.* **2013**, *23*, 4847.
[22] W. J. Chun, A. Ishikawa, H. Fujisawa, T. Takata, J. N. Kondo, M. Hara, M. Kawai, Y. Matsumoto, K. Domen, *J. Phys. Chem. B* **2003**, *107*, 1798.
[23] Z. N. Bi, X. Rodriguez-Martinez, C. Aranda, E. Pascual-San-Jose, A. R. Goni, M. Campoy-Quiles, X. Q. Xu, A. Guerrero, *J. Mater. Chem. A* **2018**, *6*, 19085.
[24] A. A. A. Darwish, E. F. M. El-Zaidia, M. M. El-Nahass, T. A. Hanafy, A. A. Al-Zubaidi, *J. Alloy Compd.* **2014**, *589*, 393.
[25] N. E. Courtier, J. M. Cave, J. M. Foster, A. B. Walker, G. Richardson, *Energy Environ. Sci.* **2019**, *12*, 396.
[26] L. Bertoluzzi, R. S. Sanchez, L. F. Liu, J. W. Lee, E. Mas-Marza, H. W. Han, N. G. Park, I. Mora-Sero, J. Bisquert, *Energy Environ. Sci.* **2015**, *8*, 910.
[27] Q. F. Dong, Y. J. Fang, Y. C. Shao, P. Mulligan, J. Qiu, L. Cao, J. S. Huang, *Science* **2015**, *347*, 967.
[28] D. S. H. Chan, J. C. H. Phang, *IEEE Trans. Electron. Dev.* **1984**, *31*, 381.
[29] A. Jain, A. Kapoor, *Sol. Energy Mater. Sol. Cells* **2004**, *81*, 269.
[30] R. Steim, T. Ameri, P. Schilinsky, C. Waldauf, G. Dennler, M. Scharber, C. J. Brabec, *Sol. Energy Mater. Sol. Cells* **2011**, *95*, 3256.